Robust Triboelectric Nanogenerator Based on Rolling Electrification and Electrostatic Induction at an Instantaneous Energy Conversion Efficiency of ~55%

Long Lin,[†,§] Yannan Xie,[†,§] Simiao Niu,[†] Sihong Wang,[†] Po-Kang Yang,[†] and Zhong Lin Wang[*,†,‡]

[†]School of Materials Science and Engineering, Georgia Institute of Technology, Atlanta, Georgia 30332-0245, United States and [‡]Beijing Institute of Nanoenergy and Nanosystems, Chinese Academy of Sciences, Beijing 100083, China. [§]These authors contributed equally to this work.

ABSTRACT In comparison to in-pane sliding friction, rolling friction not only is likely to consume less mechanical energy but also presents high robustness with minimized wearing of materials. In this work, we introduce a highly efficient approach for harvesting mechanical energy based on rolling electrification and electrostatic induction, aiming at improving the energy conversion efficiency and device durability. The rolling triboelectric nanogenerator is composed of multiple steel rods sandwiched by two fluorinated ethylene propylene (FEP) thin films. The rolling motion of the steel rods between the FEP thin films introduces triboelectric charges on both surfaces and leads to the change of potential difference between each pair of electrodes on back of the FEP layer, which drives the electrons to flow in the external load. As power generators, each pair of output terminals works independently and delivers an open-circuit voltage of 425 V, and a short-circuit current density of 5 mA/m^2. The two output terminals can also be integrated to achieve an overall power density of up to 1.6 W/m^2. The impacts of variable structural factors were investigated for optimization of the output performance, and other prototypes based on rolling balls were developed to accommodate different types of mechanical energy sources. Owing to the low frictional coefficient of the rolling motion, an instantaneous energy conversion efficiency of up to 55% was demonstrated and the high durability of the device was confirmed. This work presents a substantial advancement of the triboelectric nanogenerators toward large-scope energy harvesting and self-powered systems.

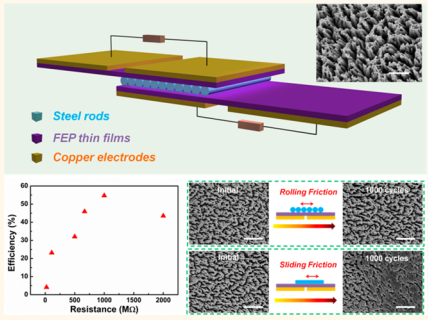

KEYWORDS: energy harvesting · triboelectric nanogenerator · robust · high efficiency · rolling electrification

Energy harvesting from the ambient environment is likely to play an important role for the sustainable development of modern society due to the consumption of traditional fossil fuels and the related environmental issues. Many endeavors have been devoted to development of renewable energy technologies that are based on various mechanisms including electromagnetic induction,[1,2] thermoelectric effects,[3,4] electrochemical reactions,[5,6] photoelectric effects,[7,8] and piezoelectric effects,[9,10] *etc*. Among numerous forms of energy sources, mechanical energy has attracted long-lasting attentions for its universal availability and extensive energy scales from human body movement to automobiles and even oceanic waves. In this regard, a novel approach of triboelectric nanogenerator (TENG)[11−18] has been recently invented that employs the coupling effect of triboelectrification[19−22] and electrostatic induction for mechanical energy harvesting. Both high output power[17,18] and numerous practical applications have been demonstrated, such as driving portable electronics,[23,24] charging energy storage units,[15] electrochemical applications,[14] and self-powered sensors,[25−28] indicating a promising potential of the TENG as a new energy technology for large scale power conversion. Up to now, four different working modes of the TENGs have been developed to accommodate applications in various types of mechanical motions, including the contact mode,[14,15,29] the sliding mode,[30,31] the single-electrode

* Address correspondence to zlwang@gatech.edu.

Received for review November 22, 2014 and accepted December 30, 2014.

Published online January 02, 2015
10.1021/nn506673x

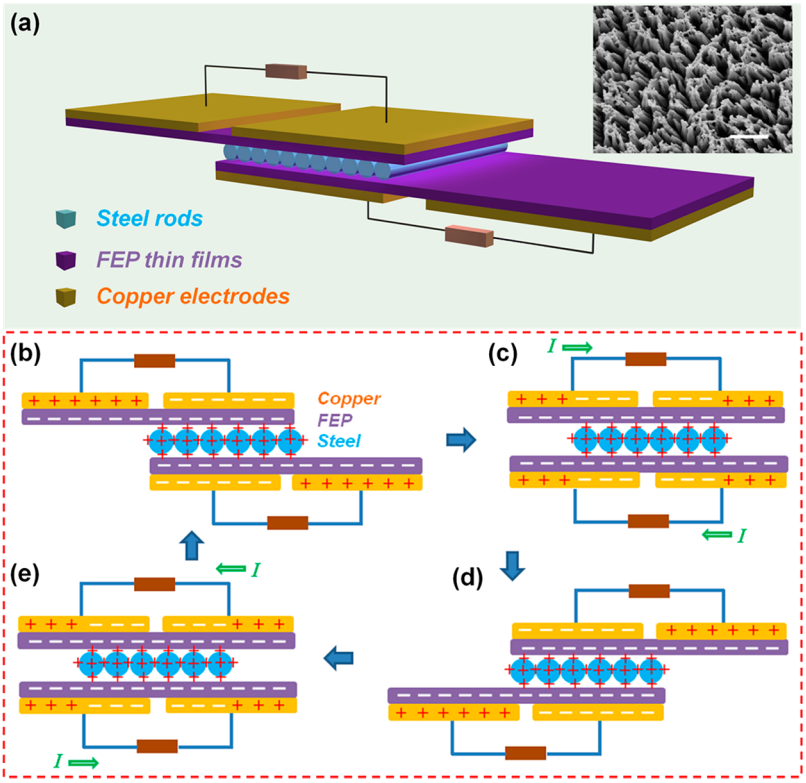

Figure 1. Structure and working principle of the rolling triboelectric nanogenerator. (a) Schematic illustration showing the device structure of the RTENG. Inset (top right): the scanning electron microscopy (SEM) image of the nanowire structure created on the inner surface of the FEP thin film. The scale bar is 1 μm. (b–e) Step-by-step illustration showing the working principle of the RTENG.

mode,[32] and the freestanding mode.[33] However, as an energy harvesting approach, the energy conversion efficiency and device durability are still essential issues, which may be limited by the relatively large frictional resistive force between triboelectric surfaces during the operation of the TENG, especially for the working modes based on sliding electrification. To improve the efficiency of the TENG and the robustness of the surface for antiwearing purpose, most efforts have been focused on enhancing the output power through sophisticated structural designs[17,18] or surface modification.[13]

In this work, we designed a novel working mode of rolling triboelectric nanogenerators (RTENG) that can deliver ultrahigh energy conversion efficiency without scarifying its robustness and stability. For the first time, rolling electrification between cylinder-shaped steel rods and planar thin films of fluorinated ethylene propylene (FEP) was employed for converting the kinetic energy of rolling rods into electric power. The rolling triboelectric nanogenerator (RTENG) has a sandwiched structure composed of two FEP thin films and steel rods rolling between them. The rolling motion of the steel rods between the FEP thin films introduces triboelectric charges on both surfaces and led to the change of potential difference between each pair of electrodes on the back of the FEP layer, which drives the electrons flow in the external load. As power generators, each pair of output terminals can work independently to deliver an open-circuit voltage of 425 V, an instantaneous charge transfer of 0.145 μC, and a short-circuit current density of 5 mA/m^2. The two sets of output terminals can also be integrated to present an overall power density of up to 1.6 W/m^2. The impact of variable structural factors were investigated to achieve optimization of the output performance, such as the velocity of the rolling motion, the gap distance between adjacent electrodes, and the diameter of the steel rods. Owing to the low friction coefficient of the rolling movement, a high energy conversion efficiency of up to 55% has been demonstrated, with much smaller wearing of triboelectric surfaces as compared with sliding friction. On the basis of the basic concept of rolling electrification, many other prototypes of RTENGs have been successfully derived, like the rotating disk structure, the grating structure, and other structures based on rolling balls. This work demonstrates a new working mode of highly efficient and robust TENGs toward large-scale energy harvesting.

RESULTS AND DISCUSSION

The device structure of the RTENG is schematically illustrated in Figure 1a, which is composed of a group of rolling steel rods sandwiched by two layers of FEP thin films. Each FEP thin film was deposited with two separated copper electrodes on its back side,

respectively. Polymer nanowire structures were created on both inner surfaces of the FEP thin film through inductively coupled plasma (ICP) etching to enhance the tribo-charge density upon rolling electrification. During the operation of the RTENG, the bottom layer FEP film (BL-FEP) was securely attached onto a three-dimensional stage, and the top layer FEP film (TL-FEP) was driven by a linear motor to oscillate back and forth, which also initiated the rolling motion of the steel rods. As the TL-FEP moved from the left end to the right end of the BL-FEP, the steel rods would also move from the left part to the right part of the BL-FEP, until the TL-FEP stopped and started to move back. Figure 1b–e depicts the working principle of the RTENG-based on a step-by-step analysis of the charge-transfer process. As the steel rods make contact with the entire area of both FEP films, due to their different abilities in attracting electrons, there will be net negative charges on the inner surface of the FEP films and net positive charges on the surface of the steel rods. By assuming even distribution of the negative charges on the FEP surface and the symmetric layout of the electrodes, the negative charges will not lead to electric output, and the potential difference between each pair of electrodes will only rely on the relative location of the positively charged steel rods. Initially (Figure 1b), the positively charged steel rods are located beneath the right-hand electrode (RE) of the TL-FEP, and over the left-hand electrode (LE) of the BL-FEP. Hence, for the top layer, the RE poses a higher electrical potential than the LE, leading to an instantaneous electrons flow from the LE to the RE to reach an equilibrium state. The opposite potential polarity (the potential of the LE is higher than that of the RE) exists in the bottom layer. As the TL-FEP starts to slide toward the right side along with the positively charged steel rods, the potential difference between the RE and the LE on the top layer will be gradually reduced until it reaches the equal potential conditions in Figure 1c. As the TL-FEP continues moving forward, the electrical potential on the LE will be higher than that of the RE, and the potential difference will reach the maximum when the TL-FEP stops at the right side of the BL-FEP (Figure 1d). In the next half cycle of rolling motion, the TL-FEP moves back from the right side to the left side, and the potential difference between the LE and the RE first drops to zero (Figure 1e) and then becomes negative until it reaches the original position (Figure 1b). In this process, due to the movement of the positively charged rolling rods in reference to the BL-FEP, the revolution of potential difference in the bottom pair of electrodes will follow a reverse trend as compared to the top layer. In terms of the short-circuit condition, the change of potential difference in the first half cycle of motion will lead to electron flow from the RE to the LE in the top layer, and the electrons will flow back from the LE to the RE in the second half cycle. Similar to the revolution of potential difference, the short-circuit electrons flow follows an opposite direction in the bottom layer as compared to the top layer.

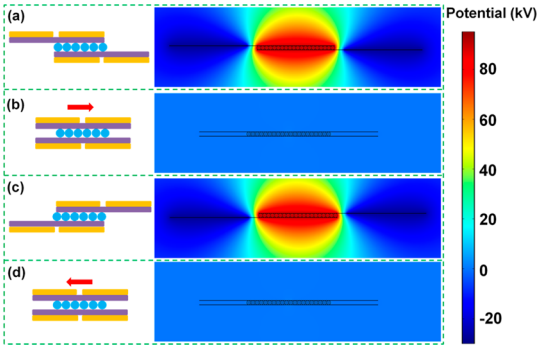

Figure 2. Numerical calculations of the potential distribution across the electrodes of the RTENG. (a) Calculated potential distribution when the rolling rods are on the left part of the bottom layer. (b) Calculated potential distribution when the rolling rods slide toward the right part of the bottom layer. (c) Calculated potential distribution when the rolling rods are on the right part of the bottom layer. (d) Calculated potential distribution when the rolling rods slide back to the left part of the bottom layer.

To gain a more quantitative understanding about the working mechanism of the RTENG, a finite element method (FEM)[34,35] was utilized to calculate the open-circuit potential distribution between the two electrodes at different states of motion. In the established two-dimensional model, a pair of FEP thin films with a length of 85 mm and a thickness of 100 μm was selected, and each pair of copper electrodes on the back side of the FEP were separated with a 5 mm gap. Twenty steel rods with a diameter of 2 mm were sandwiched between the two FEP films, which were assigned a triboelectric charge density of 60 μC/m^2. The reference state was selected as the condition that the electric potential was zero at infinity. The calculated potential distribution is shown in Figure 2a–d, which corresponds to the four different states in Figure 1b–e. From the calculation results, it can be found that the revolution of potential distribution on both pairs of electrodes is consistent with what is proposed in the schematic working mechanism. Taking the electrodes on the top layer as an example, the potential on the RE is much higher than that on the LE at the first state when the steel rods are located beneath the RE of the top layer (Figure 2a). As the steel rods roll to the middle position between the LE and RE, an equal-potential state is achieved (Figure 2b). The potential difference between the RE and LE becomes negative when the rolling rods are located beneath the left side of the top layer (Figure 2c). The other equal-potential state will be obtained when the top layer moves back and reaches the middle position of the two electrodes (Figure 2d), which is similar to the condition of Figure 2b. When it comes to the electrodes on the bottom layer, an opposite polarity but the same magnitude of potential difference can be calculated. The highest potential

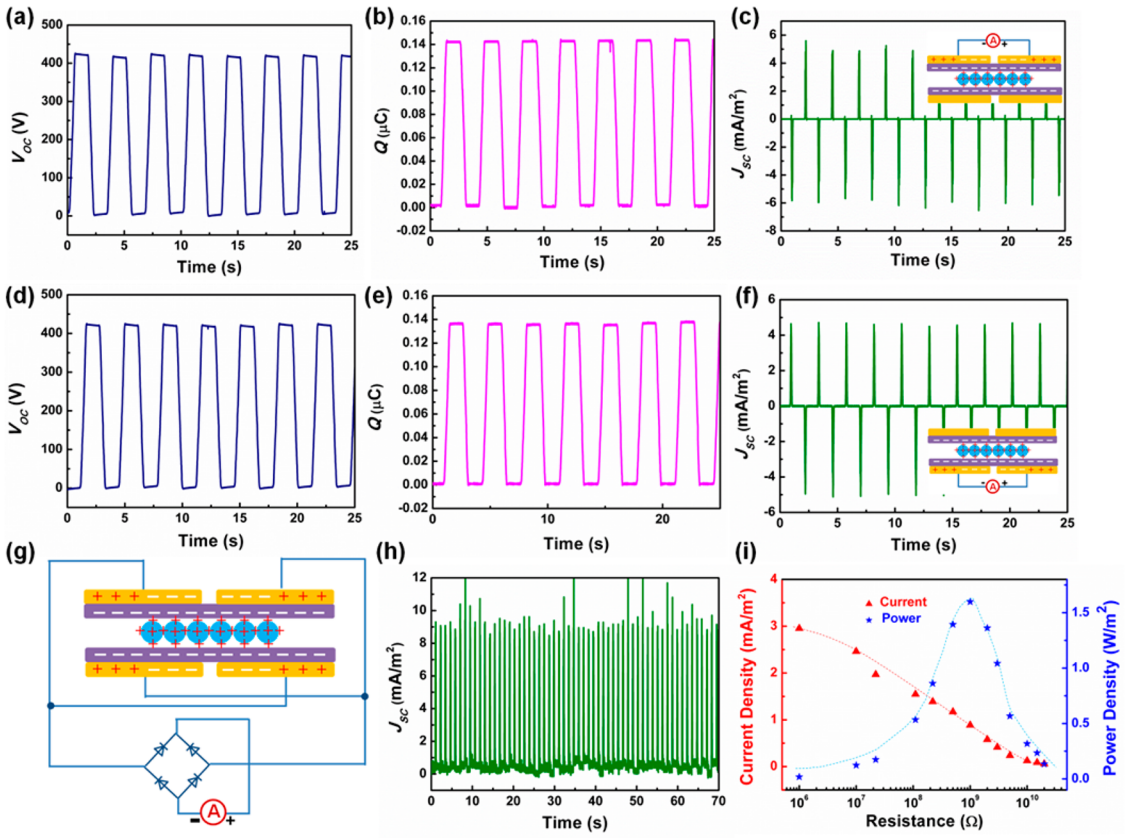

Figure 3. General output performance characterization of the RTENG. (a−c) Measurement results of the open-circuit voltage, amount of transferred charges, and short-circuit current density of the RTENG from the top output terminals, respectively. Inset of c: connection polarity for the measurement of the short-circuit current. (d−f) Measurement results of the open-circuit voltage, amount of transferred charges, and short-circuit current density of the RTENG from the bottom output terminals, respectively. Inset of f: the connection polarity for the measurement of the short-circuit current. (g) Schematic showing the polarity of connection to integrate and rectify the output current from both the top and bottom output terminals. (h) Measured short-circuit current density after integration and rectification from the top and bottom output terminals. (i) Measured output current and output power with variable load resistances.

difference can reach up to 100 kV, which is a substantial driving force for the external charge flow.

There are two sets of output terminals in the RTENG, and they can work well independently, as demonstrated in the output performance characterizations in Figure 3. The measurement results of the open-circuit voltage (V_{oc}), amount of transferred charges (Q), and short-circuit current density (J_{sc}) of the output terminals on the top layer are displayed in parts a−c, respectively, of Figure 3. It can be observed that despite the relatively low contact area between the rolling rods and the planar surface of the FEP film, the top layer of the RTENG can deliver high output performance as V_{oc} = 425 V, Q = 0.145 μC, and J_{sc} = 5 mA/m^2. Figure 3d−f shows the measured output performance from the output terminals of the bottom layer, and results of similar magnitude could be obtained. For the measurement of the J_{sc}, it should be noted that both of the left electrodes were connected to the positive end of the measurement probe (insets of Figure 3c,f), and the measurement results indicate reverse polarity, which is consistent with the proposed direction of charge flow and further demonstrates the validity of the working principle. Furthermore, it seems that the output current of the bottom layer is a little more stable than that of the top layer, which might be because the bottom electrodes are stationary while the top electrodes undergo reciprocating movement with the TL-FEP. The two sets of output terminals can be further integrated and rectified for higher output current and convenient applications, as shown in the schematic circuit diagram in Figure 3g, where the LE of the top layer and the RE of the bottom layer were connected, and vice versa. The integrated Jsc can reach up to 9−10 mA/m^2, which almost doubles the output current density from a single layer (Figure 3h). The output current was also measured with different resistances connected in the load, and an optimum output power density of ∼1.6 W/m^2 was delivered (Figure 3i).

In order to achieve a comprehensive understanding about the working performance of the RTENG, the dependences of the output performance on various structural parameters were investigated, including the sliding velocity, the electrode separation distance, and the diameter of the rolling rods, as shown in Figure 4. For convenience, all of the measurements in this

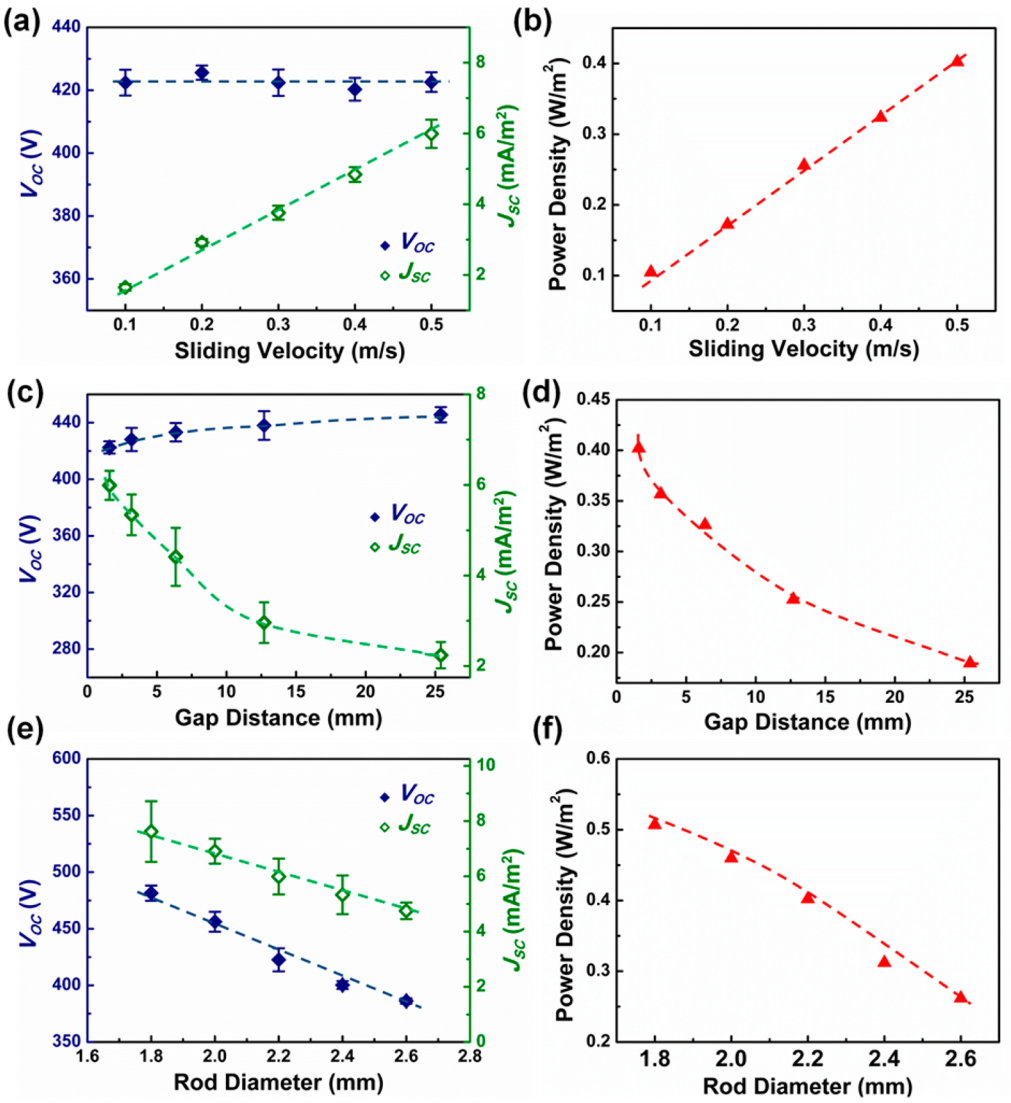

Figure 4. Dependences of the output performance of the RTENG on variable structural parameters. (a) Impact of the sliding velocity on the open-circuit voltage and the short-circuit current density of the RTENG. (b) Impact of the sliding velocity on the optimum output power density of the RTENG. (c) Impact of the gap distance between two electrodes on the same FEP thin film on the open-circuit voltage and the short-circuit current density of the RTENG. (d) Impact of the gap distance on the optimum output power density of the RTENG. (e) Impact of the rod diameter on the open-circuit voltage and the short-circuit current density of the RTENG. (f) Impact of the rod diameter on the optimum output power density of the RTENG.

section were carried out on the bottom output terminals. First, with other parameters kept constant, the output performances with variable sliding velocities were measured (Figure 4a,b), and it can be found that while the V_{oc} remains unchanged with the sliding velocity, the J_{sc} is raised with increasing velocities from 0.1 to 0.5 m/s. The different trends can be attributed to the fact that the V_{oc} is a static signal that only depends on the amount of tribo-charges and the magnitude of the charge separation; on the other hand, the J_{sc} is a dynamic signal that is also highly proportional to the rate of the charge-transfer process. Hence, the maximum output power also increases with the sliding velocity. Second, with the horizontal separation distance between two electrodes on each FEP thin film increasing from 1.6 to 25.4 mm, the V_{oc} shows a slight enhancement, but the J_{sc} decays drastically. Theoretically, the V_{oc} should have increased with the elevation of gap distance, since a larger distance between the two electrodes leads to a smaller capacitance, which is inversely proportional to the V_{oc} with constant amount of transferred charges; however, this increasing trend can hardly be recorded due to the nonideal inner resistance of the voltage meter.[33] The increase of the separation distance also results in longer time for the charge-transfer process and hence lower J_{sc}, which is consistent with the measurement results. on the basis of these results, it is easy to understand that total power output declines with larger gap distance. Third, as displayed in Figure 4e,f, both the V_{oc} and J_{sc} decrease with the elevation of the diameter of the rolling rods. Assuming constant charge density on the steel

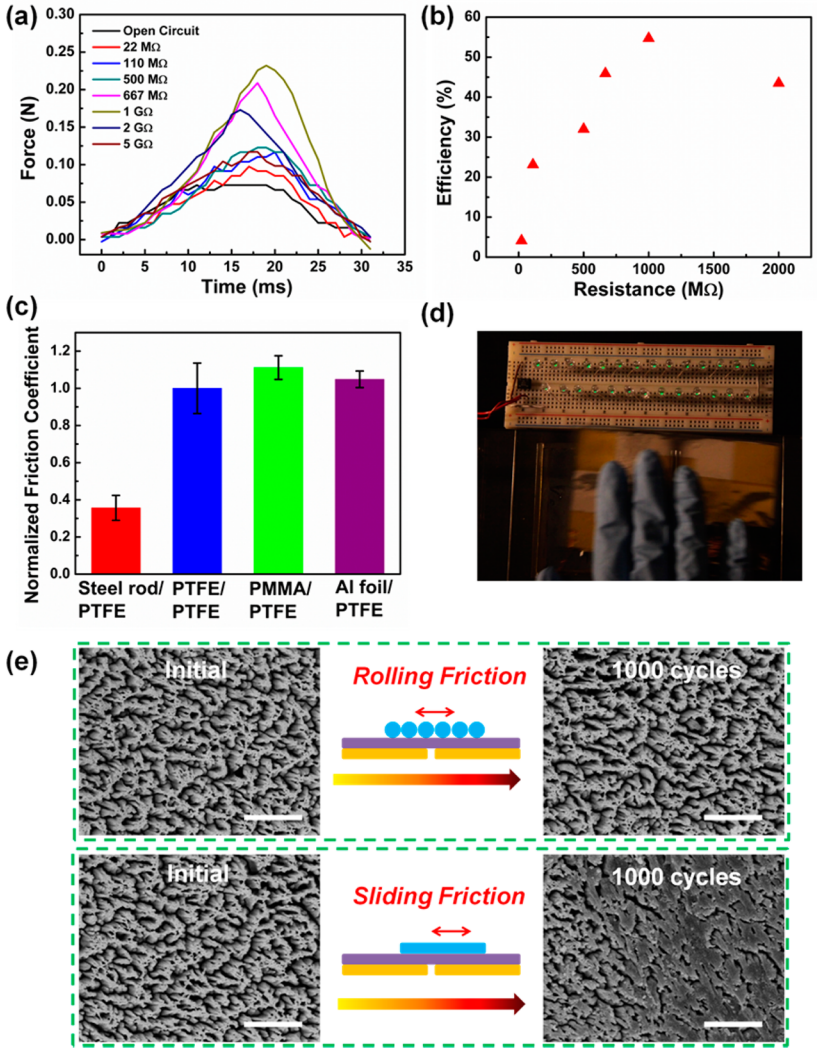

Figure 5. Characterization of the energy conversion efficiency of the RTENG. (a) Measurement of the resistive force during the energy conversion process of the RTENG with variable loading resistances. (b) Calculated energy conversion efficiency with variable load resistances. (c) Normalized friction coefficient between different types of materials customized for triboelectric nanogenerators. The friction coefficient between PTFE films were set as the reference value. (d) Capture of live demonstration indicating the instantaneous powering of portable electronics by the RTENG. (e) Comparison of the impact of surface morphology between rolling friction steel rods (top) and sliding friction by steel foils (bottom). The left two SEM images show the surface morphologies of the two samples before the friction and the right two SEM images show the surface morphologies after the friction, respectively. The scale bars are 2 μm for all images.

rods with variable diameters, the surface charges on each single rod can be considered as equivalent charge centers at axial line of the cylinder structure. Hence, as the diameter of the rolling rods grows larger, the distance between the charge center and the electrodes keeps increasing, which renders lower potential difference than that with the smaller rolling rods. All in all, combining the results demonstrated by Figure 4c–f, it can be concluded that lower rod size and gap distance are favorable for the overall output performance of the RTENG.

The rolling rod structure was utilized to minimize the frictional force in the power generator without scarifying the output power, and thus, it may enhance the energy conversion efficiency. In this regard, the energy conversion efficiency was evaluated by measurement of the resistive force in both open-circuit condition and variable load resistances.[17] It can be found that the resistive force became larger when load resistances were connected (Figure 5a), for the reason that the current flow or energy consumption in the load will yield higher electrostatic resistance to the rolling motion. Hence, by assuming constant frictional energy loss from heat dissipation, the energy conversion efficiency could be calculated by the amount of additional work done with external load divided by the total work through the following equation:

$$\eta = \frac{E_{output}}{E_{input}} = \frac{\int F dt - \int F_0 dt}{\int F dt} \quad (1)$$

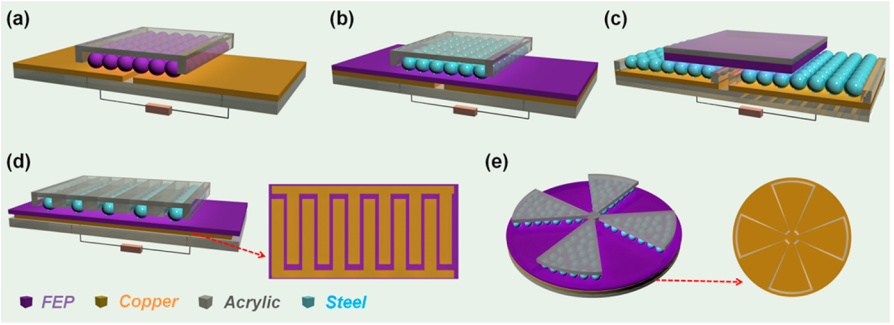

Figure 6. Schematic structure of the configurations of the rolling TENGs. (a) Schematic structure of the RTENG based on the rolling electrification between a group of PTFE balls and two separated copper electrodes. (b) Schematic structure of the RTENG based on the rolling electrification between a group of steel balls and a piece of FEP film deposited by two separated copper electrodes. (c) Schematic structure of the RTENG based on the rolling electrification between two groups of steel balls and a piece of freestanding FEP film. (d) Schematic structure of the RTENG based on the rolling electrification between several strips of steel balls and a piece of FEP film deposited by two sets of complementary grating copper electrodes. Inset: detailed structure of the grating electrodes. (e) Schematic structure of the RTENG for rotational mechanical energy harvesting. This type of RTENG is composed of rolling balls distributed into four segments of a patterned disk structure and a piece of disk-shaped FEP film deposited with two complementary copper electrodes, as shown in the inset image. The measured output performances of these prototypes are discussed in the Supporting Information.

Here, η is the energy conversion efficiency, E_{output}, is the electrical energy output, E_{input}, is the mechanical energy input, F is the resistive force measured with a certain load resistance, and F_0 is the resistive force measured with open-circuit conditions. The calculation results are displayed in Figure 5b, indicating that the instantaneous efficiency can be up to 55% when the external resistance of the load is compatible with the internal impedance of the RTENG at current motion status. This energy conversion efficiency is different from the total energy conversion efficiency defined previously[36] that accounts all of the electricity generated by the residual vibration of the device. The high energy conversion efficiency can be attributed to the low frictional coefficient between the rolling rods and the planar FEP surface, which is considered a unique advantage of this design. From the measurement of normalized friction coefficient (Figure 5c), it can be found that the frictional coefficient of the rolling rod structure is substantially lower than that of the planar structures. This high-efficient RTENG could be employed for harvesting energy from gentle finger movement, which was then utilized for driving portable electronics, like light-emitting diodes (Figure 5d and video S1, Supporting Information). Furthermore, the durability of the RTENG was verified by monitoring the surface morphology of the polymer nanowire structures over a long period of operations, as shown in Figure 5e. Two samples of the nanostructured FEP thin films were set up to undergo the rolling friction and sliding friction for 1000 cycles, respectively. The scanning electron microscopy (SEM) images of both samples were taken before and after the rolling or sliding frictions. It is clearly indicated that the sample applied with rolling friction had little degradation in the nanowire structures, while the most of the nanowires on the other sample enduring sliding friction were destroyed by the frictional force. With this comparison, the high durability of the RTENG was successfully demonstrated, which confirmed another unique advantage of the RTENG as compared to the traditional sliding TENGs.

In addition to the basic structure of the above-mentioned RTENG, the concept of rolling electrification was further explored with other prototypes based on rolling balls, as presented in Figure 6, and the measurement results of their output performances are displayed in Figures S1−5 (Supporting Information). The first three configurations are basic structures employing the rolling electrification between a group of rolling balls and planar thin films. Figure 6a shows the schematic structure of the first configuration. A group of dielectric PTFE balls are confined by an acrylic bracket, and they get negatively charged upon contact with the underlying copper electrodes. The PTFE balls are allowed to freely roll between the pair of copper electrodes, which induces change of potential difference between the two electrodes and the charge flow in the external load. Parts b and c of Figure 6 exhibit another two types of rolling-ball-based RTENG with a similar working principle as described in Figure 6a. Specifically, the configuration in Figure 6b utilizes the rolling electrification between steel balls and planar FEP thin film, and the potential difference change will be induced on the pair of copper electrodes on the back side of the FEP thin film. In Figure 6c, two separate sets of steel rods are directly connected with the underlying copper electrodes, and a freestanding FEP thin film will be rolling between the two groups of balls to generate electric power. The measured output performances of these three configurations are similar in profile and magnitude (Figures S1−S3, Supporting Information), but lower than that demonstrated in the rolling-rods-based structure. One possible reason might be the relatively lower contact area

between the rolling balls and the planar films. To further enhance the performance of the rolling-ball-based TENG, two advanced designs were fulfilled including the linear-grating RTENG (Figure 6d) and the disk-rotation RTENG (Figure 6e). As revealed by Figure 6d, the steel balls are confined in several separate strips, and the concurrent movement of the rolling balls will introduce potential difference between the two sets of copper electrodes. With this configuration the output current is improved due to a larger rate of charge transfer, and more importantly, multiple cycles of charge transfer can be achieved through one single cycle of reciprocating movement (Figure S4, Supporting Information). In the disk-rotation RTENG as shown in Figure 6e, the rolling balls are confined in several parts of a disk-patterned acrylic bracket, and the underlying FEP thin film is deposited by complementary disk-patterned electrodes. This configuration was designed to accommodate the energy harvesting from rotating motions with tunable frequency, and the output current can be further employed for self-powered angular speed sensor based on the linear relationship between the magnitude of current output and the rotation speed (Figure S5d,e, Supporting Information).

CONCLUSIONS

In summary, a high-efficient and robust approach for energy harvesting was demonstrated based on rolling electrification with much lower resistive force. Due to asymmetric screening of the triboelectric charges on the steel rods, a potential difference is induced between each two electrodes on the back of the FEP thin film, which is the driving force for the external charge flow. On the basis of this basic working principle, a high output power of 1.6 W/m^2 and an excellent instantaneous energy conversion efficiency of up to 55% were demonstrated, due to very low frictional energy loss during the operation of the RTENG. The durability of the device was verified through tracking the surface morphology by SEM, indicating tremendously low wearing of materials. A comprehensive investigation was conducted to figure out the parameter effects on the output power of the rolling nanogenerator. Various other prototypes based on rolling spheres and different structural designs were also successfully fabricated to convey the basic concept of rolling electrification for effective and efficient energy harvesting. This work presents a new mode of triboelectric nanogenerator and brings up the development of this energy technology into a new horizon.

EXPERIMENTAL SECTION

Fabrication of the Polymer Nanowire Structures on the Surface of the FEP Thin Film. A 100-μm-thick FEP thin film (American Durafilm) was cleaned with menthol, isopropyl alcohol, and deionized water consecutively and then blown dry with nitrogen gas. Then the surface of the FEP thin film was deposited with a 10-nm-thick gold thin film by sputtering (Unifilm Sputter) as the mask for the following etching to create the nanowire structures using ICP. Specifically, Ar, O_2, and CF_4 gases were introduced into the ICP chamber with the flow rate of 15.0, 10.0, and 30.0 sccm, respectively. One power source of 400 W was used to generate a high density of plasma and the other power of 100 W was used to accelerate the plasma ions. The FEP thin film was etched for 1−5 min with the above parameters.

Assembly of the Rolling Triboelectric Nanogenerator. First, two 0.125-in.-thick acrylic sheets were processed by laser cutting (PLS6.75, Universal Laser Systems) to form the two rectangular cyclostyles with the dimension of 85 mm × 50 mm as supporting substrates. The FEP thin films prepared in the above-mentioned process were then deposited with two copper electrodes separated by an acrylic mask in the middle of the thin film on its back side. The FEP thin films were then attached onto the two acrylic templates with each electrode connected to an electrical lead for measurement. Twenty steel rods with smooth surface were placed between the two inner surfaces of the FEP thin films, enabling the top layer to move against the bottom layer with low friction.

Electrical Measurement of the Rolling Triboelectric Nanogenerator. In the electrical output measurement, the top layer (moving part) of the RTENG was bonded onto a linear motor, and the bottom layer (stationary part) was secured on a stationary XYZ linear translation stage (462-XYZ-M, Newport Inc.). The open-circuit voltage and transferred charge density were measured by a Keithley 6514 System Electrometer, and the short-circuit current was measured by an SR570 Low Noise Current Amplifier (Stanford Research System).

Conflict of Interest: The authors declare no competing financial interest.

Supporting Information Available: Video recording the live demonstration of the RTENG to power up LEDs; measured output performances of the additional configurations of the RTENGs. This material is free of charge *via* the Internet at http://pubs.acs.org.

Acknowledgment. This research was supported by Basic Energy Sciences DOE, MURI from the U.S. Air Force, The Hightower Chair Foundation, and the "Thousands Talent" program for pioneer researchers and their innovation team.

REFERENCES AND NOTES

1. Beeby, S. P.; Torah, R. N.; Tudor, M. J.; Glynne-Jones, P.; O'Donnell, T.; Saha, C. R.; Roy, S. A Micro Electromagnetic Generator for Vibration Energy Harvesting. *J. Micromech. Microeng.* **2007**, *17*, 1257–1265.
2. El-hami, M.; Glynne-Jones, P.; White, N. M.; Hill, M.; Beeby, S.; James, E.; Brown, A. D.; Ross, J. N. Design and Fabrication of a New Vibration-Based Electromechanical Power Generator. *Sensor Actuat. A-Phys.* **2001**, *92*, 335–342.
3. Bell, L. E. Cooling, Heating, Generating Power, and Recovering Waste Heat with Thermoelectric Systems. *Science* **2008**, *321*, 1457–1461.
4. Kraemer, D.; Poudel, B.; Feng, H. P.; Caylor, J. C.; Yu, B.; Yan, X.; Ma, Y.; Wang, X. W.; Wang, D. Z.; Muto, A.; *et al.* High-Performance Flat-Panel Solar Thermoelectric Generators with High Thermal Concentration. *Nat. Mater.* **2011**, *10*, 532–538.
5. Shao, Z. P.; Haile, S. M.; Ahn, J.; Ronney, P. D.; Zhan, Z. L.; Barnett, S. A. A Thermally Self-Sustained Micro Solid-Oxide Fuel-Cell Stack with High Power Density. *Nature* **2005**, *435*, 795–798.
6. Debe, M. K. Electrocatalyst Approaches and Challenges for Automotive Fuel Cells. *Nature* **2012**, *486*, 43–51.

7. Huynh, W. U.; Dittmer, J. J.; Alivisatos, A. P. Hybrid Nanorod−Polymer Solar Cells. *Science* **2002**, *295*, 2425–2427.
8. Tian, B. Z.; Zheng, X. L.; Kempa, T. J.; Fang, Y.; Yu, N. F.; Yu, G. H.; Huang, J. L.; Lieber, C. M. Coaxial Silicon Nanowires as Solar Cells and Nanoelectronic Power Sources. *Nature* **2007**, *449*, 885–889.
9. Wang, Z. L.; Song, J. H. Piezoelectric Nanogenerators Based on Zinc Oxide Nanowire Arrays. *Science* **2006**, *312*, 242–246.
10. Wang, X. D.; Song, J. H.; Liu, J.; Wang, Z. L. Direct-Current Nanogenerator Driven by Ultrasonic Waves. *Science* **2007**, *316*, 102–105.
11. Wang, Z. L. Triboelectric Nanogenerators as New Energy Technology for Self-Powered Systems and as Active Mechanical and Chemical Sensors. *ACS Nano* **2013**, *7*, 9533–9557.
12. Fan, F. R.; Tian, Z. Q.; Wang, Z. L. Flexible Triboelectric Generator. *Nano Energy* **2012**, *1*, 328–334.
13. Fan, F. R.; Lin, L.; Zhu, G.; Wu, W. Z.; Zhang, R.; Wang, Z. L. Transparent Triboelectric Nanogenerators and Self-Powered Pressure Sensors Based on Micropatterned Plastic Films. *Nano Lett.* **2012**, *12*, 3109–3114.
14. Zhu, G.; Pan, C. F.; Guo, W. X.; Chen, C. Y.; Zhou, Y. S.; Yu, R. M.; Wang, Z. L. Triboelectric-Generator-Driven Pulse Electrodeposition for Micropatterning. *Nano Lett.* **2012**, *12*, 4960–4965.
15. Wang, S. H.; Lin, L.; Wang, Z. L. Nanoscale Triboelectric-Effect-Enabled Energy Conversion for Sustainably Powering Portable Electronics. *Nano Lett.* **2012**, *12*, 6339–6346.
16. Lin, L.; Wang, S. H.; Xie, Y. N.; Jing, Q. S.; Niu, S. M.; Hu, Y. F.; Wang, Z. L. Segmentally Structured Disk Triboelectric Nanogenerator for Harvesting Rotational Mechanical Energy. *Nano Lett.* **2013**, *13*, 2916–2923.
17. Zhu, G.; Zhou, Y. S.; Bai, P.; Meng, X. S.; Jing, Q. S.; Chen, J.; Wang, Z. L. A Shape-Adaptive Thin-Film-Based Approach for 50% High-Efficiency Energy Generation Through Micro-Grating Sliding Electrification. *Adv. Mater.* **2014**, *26*, 3788–3796.
18. Zhu, G.; Chen, J.; Zhang, T. J.; Jing, Q. S.; Wang, Z. L. Radial-Arrayed Rotary Electrification for High Performance Triboelectric Generator. *Nat. Commun.* **2014**, *5*, 3426.
19. Castle, G. S. P. Contact Charging Between Insulators. *J. Electrostat.* **1997**, *40−1*, 13–20.
20. Diaz, A. F.; Felix-Navarro, R. M. A Semi-Quantitative Tribo-Electric Series for Polymeric Materials: the Influence of Chemical Structure and Properties. *J. Electrostat.* **2004**, *62*, 277–290.
21. McCarty, L. S.; Whitesides, G. M. Electrostatic Charging Due to Separation of Ions at Interfaces: Contact Electrification of Ionic Electrets. *Angew. Chem., Int. Ed.* **2008**, *47*, 2188–2207.
22. Zhou, Y. S.; Liu, Y.; Zhu, G.; Lin, Z. H.; Pan, C. F.; Jing, Q. S.; Wang, Z. L. *In Situ* Quantitative Study of Nanoscale Triboelectrification and Patterning. *Nano Lett.* **2013**, *13*, 2771–2776.
23. Zhong, J. W.; Zhong, Q. Z.; Fan, F. R.; Zhang, Y.; Wang, S. H.; Hu, B.; Wang, Z. L.; Zhou, J. Finger Typing Driven Triboelectric Nanogenerator and Its Use for Instantaneously Lighting Up LEDs. *Nano Energy* **2013**, *2*, 491–497.
24. Zhu, G.; Bai, P.; Chen, J.; Wang, Z. L. Power-Generating Shoe Insole Based on Triboelectric Nanogenerators for Self-Powered Consumer Electronics. *Nano Energy* **2013**, *2*, 688–692.
25. Zhou, Y. S.; Zhu, G.; Niu, S. M.; Liu, Y.; Bai, P. S.; Jing, Q.; Wang, Z. L. Nanometer Resolution Self-Powered Static and Dynamic Motion Sensor Based on Micro-Grated Triboelectrification. *Adv. Mater.* **2014**, *26*, 1719–1724.
26. Lin, L.; Xie, Y. N.; Wang, S. H.; Wu, W. Z.; Niu, S. M.; Wen, X. N.; Wang, Z. L. Triboelectric Active Sensor Array for Self-Powered Static and Dynamic Pressure Detection and Tactile Imaging. *ACS Nano* **2013**, *7*, 8266–8274.
27. Zhang, H. L.; Yang, Y.; Hou, T. C.; Su, Y. J.; Hu, C. G.; Wang, Z. L. Triboelectric Nanogenerator Built Inside Clothes for Self-Powered Glucose Biosensors. *Nano Energy* **2013**, *2*, 1019–1024.
28. Zhang, H. L.; Yang, Y.; Su, Y. J.; Chen, J.; Hu, C. G.; Wu, Z. K.; Liu, Y.; Wong, C. P.; Bando, Y.; Wang, Z. L. Triboelectric Nanogenerator as Self-Powered Active Sensors for Detecting Liquid/Gaseous Water/Ethanol. *Nano Energy* **2013**, *2*, 693–701.
29. Tang, W.; Meng, B.; Zhang, H. X. Investigation of Power Generation Based on Stacked Triboelectric Nanogenerator. *Nano Energy* **2013**, *2*, 1164–1171.
30. Wang, S. H.; Lin, L.; Xie, Y. N.; Jing, Q. S.; Niu, S. M.; Wang, Z. L. Sliding-Triboelectric Nanogenerators Based on In-Plane Charge-Separation Mechanism. *Nano Lett.* **2013**, *13*, 2226–2233.
31. Zhu, G.; Chen, J.; Liu, Y.; Bai, P.; Zhou, Y. S.; Jing, Q. S.; Pan, C. F.; Wang, Z. L. Linear-Grating Triboelectric Generator Based on Sliding Electrification. *Nano Lett.* **2013**, *13*, 2282–2289.
32. Yang, Y.; Zhang, H. L.; Chen, J.; Jing, Q. S.; Zhou, Y. S.; Wen, X. N.; Wang, Z. L. Single-Electrode-Based Sliding Triboelectric Nanogenerator for Self-Powered Displacement Vector Sensor System. *ACS Nano* **2013**, *7*, 7342–7351.
33. Wang, S. H.; Xie, Y. N.; Niu, S. M.; Lin, L.; Wang, Z. L. Freestanding-Triboelectric-Layer Based Nanogenerators for Harvesting Energy from a Moving Object or Human Motion in Contact and Non-Contact Modes. *Adv. Mater.* **2014**, *26*, 2818–2824.
34. Niu, S. M.; Liu, Y.; Wang, S. H.; Lin, L.; Zhou, Y. S.; Hu, Y. F.; Wang, Z. L. Theory of Sliding-Mode Triboelectric Nanogenerators. *Adv. Mater.* **2013**, *25*, 6184–6193.
35. Niu, S. M.; Wang, S. H.; Lin, L.; Liu, Y.; Zhou, Y. S.; Hu, Y. F.; Wang, Z. L. Theoretical Study of Contact-Mode Triboelectric Nanogenerators as an Effective Power Source. *Energy Environ. Sci.* **2013**, *6*, 3576–3583.
36. Xie, Y. N.; Wang, S. H.; Niu, S. M.; Lin, L.; Jing, Q. S.; Yang, J.; Wu, Z. Y.; Wang, Z. L. Grating-Structured Freestanding Triboelectric-Layer Nanogenerator for Harvesting Mechanical Energy at 85% Total Conversion Efficiency. *Adv. Mater.* **2014**, *26*, 6599–6607.